Journal of Hydrology 638 (2024) 131534

Contents lists available at ScienceDirect

Journal of Hydrology

journal homepage: www.elsevier.com/locate/jhydrol

Research papers

Evaluating biases in Penman and Penman–Monteith evapotranspiration rates at different timescales

Yizhi Han [a], Salvatore Calabrese [b], Huihua Du [c], Jun Yin [a,*]

[a] School of Hydrology and Water Resources, Nanjing University of Information Science and Technology (NUIST), Nanjing 210044, China
[b] Department of Biological and Agricultural Engineering, Texas A&M University, 333 Spence St, College Station 77840, TX, USA
[c] State Key Laboratory of Hydrology-Water Resources and Hydraulic Engineering, Nanjing Hydraulic Research Institute, Nanjing 210029, China

ARTICLE INFO

This manuscript was handled by S. Sally Elizabeth Thompson, Editor-in-Chief, with the assistance of Ning Ma, Associate Editor.

Dataset link: https://cds.climate.copernicus.eu/cdsapp#!/dataset/reanalysis-era5-single-levels

Keywords:
Penman equation
Penman–Monteith equation
Nonlinearity
Evaporation

ABSTRACT

The Penman and Penman–Monteith equations are widely used for estimating surface evapotranspiration (ET) at regional and global scales. These nonlinear equations were derived from the turbulent transport of heat fluxes and, in theory, need to be applied to a temporal scale ranging from half hour to an hour. However, these equations have been frequently applied with hydrometeorological variables averaged at daily, monthly, and even decadal time intervals, resulting in biases due to their nonlinearities. In this study, we used global reanalysis data and Taylor expanded Penman and Penman–Monteith equations to explore their nonlinear components and the biases associated with the timescale mismatches. We found that global average biases for approximating Penman equation range from 0.72 to 1.31 mm day^{-1} from daily to annual timescales, which mainly stem from the temperature–radiation, temperature–vapor pressure deficit (VPD), and aerodynamic conductance–VPD covariances. For Penman–Monteith equation, the corresponding biases vary from 0.47 to 0.53 mm day^{-1}, which may be associated with the addition of stomatal conductance–VPD covariances. As a reference, the global averages from Penman and Penman–Monteith at hourly timescale over one year are 7.1 and 1.7 mm day^{-1}. Large biases also exist around the world across various climate zones, where one or multiple covariances between meteorological variables makes the first-order approximations of Penman and Penman–Monteith equations less accurate. This analysis serves as a reminder of nonlinearities in Penman and Penman–Monteith equations, hence the requirement of data at high temporal resolution for estimating potential or actual evapotranspiration.

1. Introduction

On average, global evapotranspiration (ET) is directly associated with approximately 82 W m^{-2} of latent heat flux, equivalent to a quarter of incoming solar radiative flux at the top of the Earth's atmosphere (Wild et al., 2017). These latent heat fluxes are critical for boundary layer dynamics, atmospheric convection, and cloud formation, playing an important role in controlling the Earth's energy balance and climate system. At regional scales, ET is an important component of the water budget, thus influencing local water resources management and ecological processes. Due to its inherent interlinkage with the latent heat flux, modeling ET requires coupling surface energy balance to the equations of turbulent heat transport. Penman (1948) linearized the Clausius–Clapeyron relation to obtain the explicit expressions for ET from wet surfaces. Monteith (1965) further extended this approach to find ET from non-wet surfaces with the assumption of saturated condition inside the stomates. Penman and Penman–Monteith equations have been widely used in various fields ranging from regional water resources management to global climate projections.

Penman and Penman–Monteith equations were derived from the turbulent transport of heat fluxes, whose time frame is from half an hour to an hour. Directly applying these equations at longer timescales may thus result in biased results due to the nonlinearities in these equations. While this problem seems obvious, it has not received much attention and is often ignored. For example, FAO modified Penman–Monteith equation (Allen et al., 1998), a standard for estimating crop water demand, is often applied at daily timescale (e.g., Cai et al., 2007; Suleiman and Hoogenboom, 2007), which is usually integrated into longer intervals for specific applications. The Climatic Research Unit (CRU) used the Penman–Monteith equation to calculate global potential evapotranspiration (PET) at monthly timescale (Harris et al., 2020). Huang et al. (2015), Wang et al. (2020), Song et al. (2023) used monthly climate model outputs to calculate global PET. Zomer

* Corresponding author.
E-mail address: jun.yin@nuist.edu.cn (J. Yin).

https://doi.org/10.1016/j.jhydrol.2024.131534
Received 4 October 2023; Received in revised form 23 April 2024; Accepted 3 June 2024
Available online 18 June 2024

et al. (2022) used climatology data averaged over 1970–2020 (Fick and Hijmans, 2017) in each month to calculate global PET and aridity, which have been extensively used in a wide range of applications.

These applications are evidences that Penman and Penman–Monteith equations have been widely used on various timescales longer than the time frame of turbulent transport of heat fluxes (hereafter the "timescale mismatch"). Direct application of Penman equation on long timescales has in fact resulted in large biases in various countries, such as China (Yang and Zhong, 2011), Australia (Perera et al., 2015), and the United States (Itenfisu et al., 2003; Suleiman and Hoogenboom, 2009). While these case studies suggest that biases associated with timescale mismatch exist, they have been mostly restricted to data comparisons without systematically explaining the reasons for these biases. More insights on the nonlinearities of the Penman or Penman–Monteith equations are needed to understand how they affect their applications in hydrometeorological studies.

Here we Taylor expanded the Penman and Penman–Monteith equations to investigate their nonlinear components and explored how they can lead to biases in evaporation predictions. There are various definitions of PET (e.g., Lhomme, 1997); here we used the term "PET" for the rate computed from Penman (or Penman-Monteith with $g_s \gg g_a$) and used the term "ET" for the rate computed from Penman-Monteith with g_s from Jarvis' equation. While in principle an analysis of the nonlinearities could be conducted purely theoretically (*e.g.*, by estimating biases for any possible time-series of meteorological variables), here we use available data to obtain actual estimates of expected biases and quantify how they vary spatially across the globe. In particular, leveraging the state-of-the-art global reanalysis data from the European Centre for Medium-Range Weather Forecasts (ECMWF) at high temporal resolutions over the world (Hersbach et al., 2020), we found that the biases when applying the Penman equation are associated with the temperature–radiation, temperature–vapor pressure deficit (VPD), and aerodynamic conductance–VPD covariances. The biases when applying the Penman–Monteith equation are relatively larger and may be also associated with stomatal conductance–VPD covariances. The rest of the article is organized as follows. In Section 2, we explained the timescales of Penman and Penman–Monteith equations, which were then expanded into Taylor series for decomposition of their nonlinear components. These components were quantified in Section 3 with reanalysis data to provide global overview of the biases for approximating Penman and Penman–Monteith equation at different timescales. The conclusions were summarized in Section 4.

2. Methods

2.1. Penman and Penman–Monteith equations

Penman (1948) found the explicit expression for ET rate from wet surfaces (or PET from hypothetical wet surfaces), $\mathcal{F}_{\mathrm{P}}$, by solving turbulence transport of latent and sensible heat flux (see Appendix A) with surface energy balance equation and linearized Clausius–Clapeyron relationship,

$$\mathcal{F}_{\mathrm{P}}(Q,T_a,g_a,V)=\underbrace{\frac{\Delta Q}{\rho_w\lambda_w(\Delta+\gamma)}}_{\mathcal{F}_{\mathrm{P,e}}(Q,T_a)}+\underbrace{\frac{\gamma E_A}{\rho_w(\Delta+\gamma)}}_{\mathcal{F}_{\mathrm{P,d}}(T_a,g_a,V)}, \tag{1}$$

and

$$E_A=\frac{\epsilon}{p_0}\rho g_a[e_{\mathrm{sat}}(T_a)-e_a]=\frac{\epsilon}{p_0}\rho g_a V, \tag{2}$$

where λ_w is latent heat of water vaporization, ρ_w is water density, $V=(e_{\mathrm{sat}}(T_a)-e_a)$ is vapor press deficit (VPD), $Q=H+\rho_w\lambda_w E$ is the available energy defined as the sum of the latent and sensible heat fluxes, E_A is drying power of the air, $\Delta=de_{\mathrm{sat}}/dT|_{T=T_a}$ is the slope of the saturation vapor pressure against air temperature, g_a is aerodynamic conductance, and γ is the psychrometric constant, which weakly depends on temperature and air pressure. Further analysis show that the daily, monthly, and annual variations of psychrometric constant have negligible impacts on the results and therefore γ is treated as a local constant in the given study area. The aerodynamic conductance can be modeled by Monin–Obukhov similarity theory with consideration of atmospheric stability conditions (see Eq. (A.3) in Appendix A). Neglecting the stability correction function could reduce the estimated evaporation by nearly 50% in the afternoon with modest instabilities, although the biases are smaller when averaged over the whole day (Mahrt and Ek, 1984).

The first term is often referred to as equilibrium evaporation, $\mathcal{F}_{\mathrm{P,e}}$, which is a function of T_a and Q, and the second term is evaporation due to the drying power of the air, $\mathcal{F}_{\mathrm{P,d}}$, which is a function of T_a, g_a, and V. While it is common to omit the bars of Reynolds average in Eqs. (1) and (2), T_a and e_a, same as those in Eqs. (A.1) and (A.2), are still Reynolds-averaged variables, and therefore the Penman equation remains valid at sub-hourly to hourly timescales (also see chapter 2 in Porporato and Yin, 2022). Note that a more accurate solution without linearizing the Clausius–Clapeyron relationship can be found by using the Lambert-W function (McColl, 2020).

For non-wet surfaces, Monteith (1965) further extended Penman's combination approach by assuming saturated water vapor pressure inside the stomates (Porporato and Yin, 2022) and using stomatal conductance, g_s, to model the reduced evaporation rate, $\mathcal{F}_{\mathrm{PM}}$, as

$$\mathcal{F}_{\mathrm{PM}}(Q,T_a,V,g_a,g_s)=\underbrace{\frac{\Delta Q}{\rho_w\lambda_w\left[\Delta+\gamma\left(1+g_a/g_s\right)\right]}}_{\mathcal{F}_{\mathrm{PM,e}}}+\underbrace{\frac{\gamma E_A}{\rho_w\left[\Delta+\gamma\left(1+g_a/g_s\right)\right]}}_{\mathcal{F}_{\mathrm{PM,d}}}, \tag{3}$$

which reduces to the Penman Eq. (1) for complete opening of stomata (*e.g.*, $g_s \gg g_a$). Similar to the Penman Eq. (1), the bars of Reynolds average in the Penman–Monteith equation are also omitted but the equation should still be applied at sub-hourly to hourly timescale. For convenience, we also split $\mathcal{F}_{\mathrm{PM}}$ into $\mathcal{F}_{\mathrm{PM,e}}$ and $\mathcal{F}_{\mathrm{PM,d}}$, corresponding to the contributions from surface available energy and vapor pressure deficit, respectively.

Applying Penman and Penman–Monteith equations at longer timescales simply by using meteorological variables at daily, monthly, or annual (DMA) time steps introduces biases. As shown in Appendix B, for any given nonlinear function, the average of the function is not the same as the function of the averages of the independent variables. The difference depends on the variances, covariances, and higher moments of the independent variables as analyzed in the next sections.

2.2. Nonlinear components of Penman and Penman–Monteith equations

The first term in the Penman equation is a bivariate nonlinear function of T_a and Q, *i.e.*, $\mathcal{F}_{\mathrm{P,e}}(T_a,Q)=f(T_a,Q)$, where for convenience the function notation f is used as an equivalent to $\mathcal{F}_{\mathrm{P,e}}$. Applying Taylor series in Appendix B to $\mathcal{F}_{\mathrm{P,e}}(T_a,Q)$ and acknowledging the second-order derivative with respect to Q is zero yields

$$\underbrace{\langle\mathcal{F}_{\mathrm{P,e}}(T_a,Q)\rangle}_{\mathrm{I}}=\underbrace{\mathcal{F}_{\mathrm{P,e}}(\langle T_a\rangle,\langle Q\rangle)}_{\mathrm{II}}+\underbrace{1/2f_{T_aT_a}\sigma^2_{T_a}}_{\mathrm{III}}+\underbrace{f_{T_aQ}\mathrm{cov}(T_a,Q)}_{\mathrm{IV}}+\underbrace{\langle\mathrm{H.O.T.}\rangle}_{\mathrm{V}}, \tag{4}$$

where the subscripts in f indicate the variables with respect to which the partial derivatives are taken. In Eq. (4), $\mathcal{F}_{\mathrm{P,e}}(T_a,Q)$ refers to equilibrium part at subhourly to hourly timescale, and $\langle\cdot\rangle$ is different from Reynolds averages and refers to the averages for given periods. Therefore, the first term, $\langle\mathcal{F}_{\mathrm{P,e}}(T_a,Q)\rangle$, is the average of $\mathcal{F}_{\mathrm{P,e}}(T_a,Q)$ at longer timescales (*e.g.*, DMA), which can be regarded as the exact value. Term II, $\mathcal{F}_{\mathrm{P,e}}(\langle T_a\rangle,\langle Q\rangle)$, as the approximation, is the function of the averages of T_a and Q at the corresponding timescales. According to

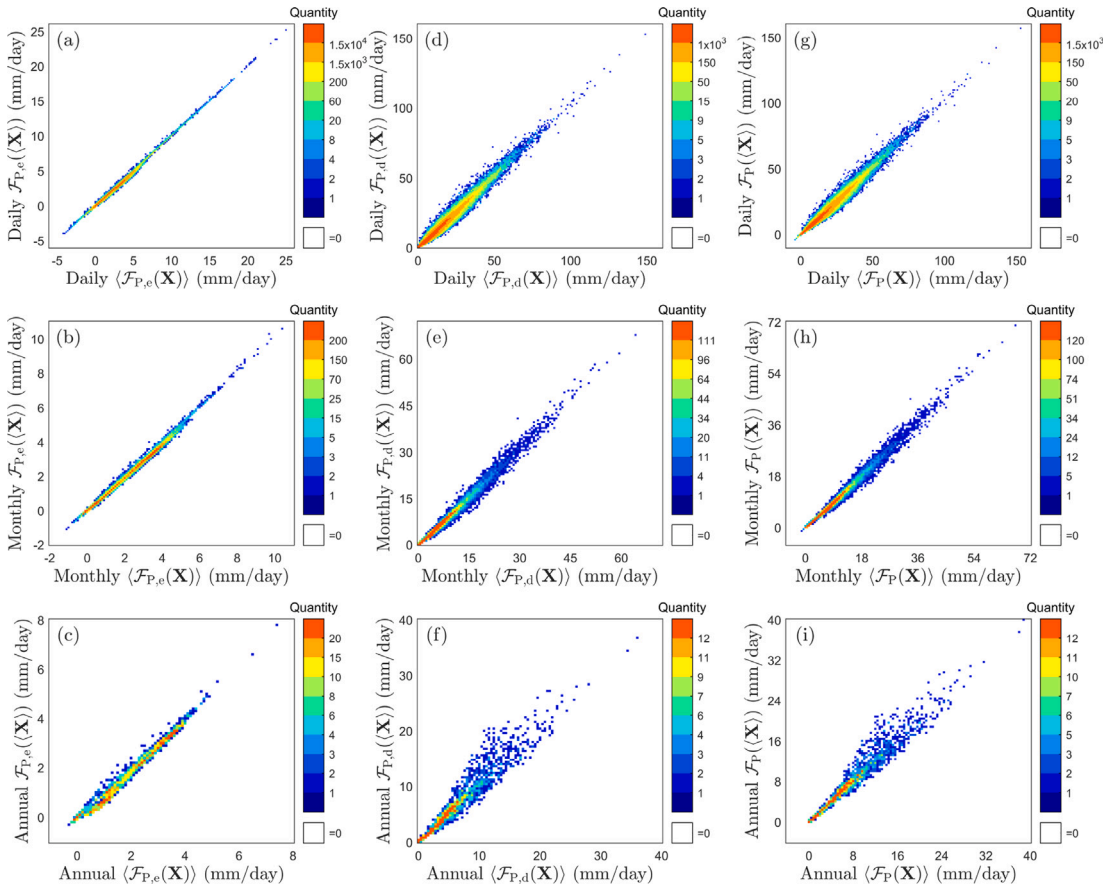

Fig. 1. Approximations of Penman equation at varying timescales. In panels (a)–(c), the exact values of equilibrium evaporation, $\langle \mathcal{F}_{P,e}(\mathbf{X}) \rangle$, are compared with first-order approximations, $\mathcal{F}_{P,e}(\langle \mathbf{X} \rangle)$, (*i.e.*, Term I vs. Term II in Eq. (4)) at the (a) daily, (b) monthly, and (c) annual scales, respectively. In panels (d)–(f), the exact values, $\langle \mathcal{F}_{P,d}(\mathbf{X}) \rangle$, are compared with the first-order approximations, $\mathcal{F}_{P,d}(\langle \mathbf{X} \rangle)$, (*i.e.*, term I vs. term II in Eq. (5)) at the (d) daily, (e) monthly, and (f) annual scales, respectively. In panels (g)–(i), the sum of $\langle \mathcal{F}_{P,e}(\mathbf{X}) \rangle$ and $\langle \mathcal{F}_{P,d}(\mathbf{X}) \rangle$ is compared with $\mathcal{F}_{P,e}(\langle \mathbf{X} \rangle)$ and $\mathcal{F}_{P,d}(\langle \mathbf{X} \rangle)$ at (g) daily, (h) monthly, and (i) annual timescales. The vector $\mathbf{X}$ refers to the list of variables in the corresponding functions; $\langle \mathcal{F}(\cdot) \rangle$ refers to the average of the function; $\mathcal{F}(\langle \cdot \rangle)$ refers to the function of the averages. Note that there are 2337 resampled locations over the global land and the total sample sizes are 365×2337, 12×2337, and 2337 at DMA timescales (also see data source in Section 2.3). The quantity color bars show the numbers of the samples.

Eq. (4), the differences between the two (*i.e.*, subtract term II from term I) depend on the temperature variances (III), temperature–radiation covariances (IV), and higher-order terms (V) (*i.e.*, the sum of all terms above second order).

The second term in the Penman equation is a function of three variables, $\mathcal{F}_{P,d}(T_a, g_a, V) = g(T_a, g_a, V)$, where for convenience the function notation g is used as an equivalent to $\mathcal{F}_{P,d}$. Considering that its second-order derivatives with respect to g_a and VPD are zeros, one can express its Taylor-series expansion as (also see Appendix B)

$$\begin{aligned} \underbrace{\langle \mathcal{F}_{P,d}(T_a, g_a, V) \rangle}_{\text{I}} = \underbrace{\mathcal{F}_{P,d}(\langle T_a \rangle, \langle g_a \rangle, \langle V \rangle)}_{\text{II}} + \underbrace{1/2 g_{T_a T_a} \sigma_{T_a}^2}_{\text{III}} \\ + \underbrace{g_{T_a g_a} \mathrm{cov}(T_a, g_a)}_{\text{IV}} + \underbrace{g_{T_a V} \mathrm{cov}(T_a, V)}_{\text{V}} \\ + \underbrace{g_{g_a V} \mathrm{cov}(g_a, V)}_{\text{VI}} + \underbrace{\langle \text{H.O.T.} \rangle}_{\text{VII}}, \end{aligned} \tag{5}$$

where the subscripts in g indicate the variables with respect to which the partial derivatives are taken. In Eq. (5), term I, $\langle \mathcal{F}_{P,d}(T_a, g_a, V) \rangle$, is the average of $\mathcal{F}_{P,d}(T_a, g_a, V)$ at longer timescales and refers to the exact values calculated from Penman equation. Term II, $g(\langle T_a \rangle, \langle g_a \rangle, \langle V \rangle)$, is the corresponding approximation. The differences between these two are therefore associated with temperature variances (III), temperature–aerodynamic conductance covariances (IV), temperature–VPD covariances (V), aerodynamic conductance–VPD covariances (VI), and higher-order terms (VII).

For Penman–Monteith equation, it is a function of five variables, and subsequently its Taylor series to the second order can be as many as 16 terms, complicating the decomposition of the biases. In this regard, we only expand it to the first order around the averages as

$$\langle \mathcal{F}_{PM}(Q, T_a, V, g_a, g_s) \rangle = \mathcal{F}_{PM}(\langle Q \rangle, \langle T_a \rangle, \langle V \rangle, \langle g_a \rangle, \langle g_s \rangle) + \langle \text{H.O.T.} \rangle, \tag{6}$$

where $\langle \mathcal{F}_{PM}(Q, T_a, V, g_a, g_s) \rangle$ refers to the exact values and $\mathcal{F}_{PM}(\langle Q \rangle, \langle T_a \rangle, \langle V \rangle, \langle g_a \rangle, \langle g_s \rangle)$ is the first-order approximation. We will take advantage of the global reanalysis data and attempt to diagnose the nonlinear components of this Penman–Monteith equation by comparing its bias (*i.e.*, $\langle \text{H.O.T.} \rangle$) with the covariances between different variables.

2.3. ERA-5 global reanalysis data

To quantify the importance of each term in Eqs. (4), (5), and (6), we used the latest state-of-the-art reanalysis of ERA-5 produced at ECMWF (datasets are available at https://cds.climate.copernicus.eu/cdsapp#!/dataset/reanalysis-era5-single-levels). ERA-5 reanalysis datasets with global coverage and continuous meteorological variable outputs at hourly timescale have shown great promise in capturing the diurnal and seasonal cycles of surface heat fluxes (Hoffmann et al., 2019; Hersbach et al., 2020; Dai, 2023). From ERA-5, latent and sensible heat fluxes were combined as the available energy, Q, air temperature at 2 meters is used for variable T_a, dew point temperature (T_d) and air temperature were used to estimate vapor pressure deficit using Clausius–Clapeyron relationship, $V = e_{sat}(T_a) - e_{sat}(T_d)$, and g_a and

Table 1
Bias statistics of Penman and Penman–Monteith equations. The vector, **X**, refers to the list of variables in the corresponding functions.

Time scales	Statistics	$\langle \mathcal{F}_{P,e}(\mathbf{X})\rangle$ vs. $\mathcal{F}_{P,e}(\langle \mathbf{X}\rangle)$	$\langle \mathcal{F}_{P,d}(\mathbf{X})\rangle$ vs. $\mathcal{F}_{P,d}(\langle \mathbf{X}\rangle)$	$\langle \mathcal{F}_{P}(\mathbf{X})\rangle$ vs. $\mathcal{F}_{P}(\langle \mathbf{X}\rangle)$	$\langle \mathcal{F}_{PM}(\mathbf{X})\rangle$ vs. $\mathcal{F}_{PM}(\langle \mathbf{X}\rangle)$
Daily	RMSB	0.12	0.87	0.90	0.53
	MAB	0.09	0.44	0.48	0.30
	MB	0.08	0.13	0.22	0.28
Monthly	RMSB	0.12	0.70	0.72	0.47
	MAB	0.09	0.38	0.40	0.29
	MB	0.08	0.04	0.12	0.25
Annual	RMSB	0.22	1.41	1.31	0.47
	MAB	0.18	0.77	0.74	0.33
	MB	0.16	−0.39	−0.23	0.23

g_s were estimated by Eqs. (A.3) and (A.4). Note that the Monin–Obukhov length in Eq. (A.3) was numerically solved in an implicit equation between stability parameter and bulk Richardson number with estimated surface heat fluxes outputs from ERA-5 (ECMWF, 2023). Our analysis was conducted over a typical year of 1994, when neither El Niño nor La Niña conditions were strong. To make it computationally less expensive, the original ERA-5 data with 0.25° latitude–longitude grids were resampled into 2337 equal-area grids over the land using the nearest neighbor interpolation method, which preserves more information regarding the spatial variability of meteorological variables without using spatial smoothing methods and provides a rough representation of global conditions. It should be noted the methods proposed here for analyzing the nonlinearities of Penman and Penman–Monteith equations should not be limited to reanalysis data. However, obtaining high-resolution global meteorological variables remains a challenge. For instance, no FLUXNET records (Pastorello et al., 2020) are available if any low-quality data (qc ≥ 1) is excluded.

3. Results and discussions

3.1. Nonlinearity of Penman equation

We substituted hourly T_a and Q from ERA-5 into Eq. (1) to calculate hourly $\mathcal{F}_{P,e}$ for the equilibrium part of the Penman equation and then averaged at DMA scales to obtain exact values of evaporation. Since the land surface is not always wet, the results calculated from the Penman equation only refer to the PET as the atmospheric water demand. The hourly data were also used to calculate the variance and covariance (*i.e.*, $\sigma^2_{T_a}$ and $\mathrm{cov}(T_a, Q)$) at DMA scales. Finally, these values were used to calculate each term in Eq. (4) to assess the nonlinearity of the equilibrium part of the Penman equation. Note that term V is calculated as the residual of the whole equation, *i.e.*, Term V = Term I − Term II − Term III − Term IV.

As shown in Fig. 1 a–c, the approximations (*i.e.*, term II, $\mathcal{F}_{P,e}(\langle T_a\rangle, \langle Q\rangle)$) at daily and monthly timescales are quite close to the exact value (*i.e.*, term I, $\langle \mathcal{F}_{P,e}(T_a, Q)\rangle$), and only become less accurate at annual timescales (see statistics in Table 1). To quantify the importance of each term in Eq. (4), we plotted each term against the total biases (*i.e.* Term III+IV+V) in Fig. 2. As can be seen, the T_a-Q covariance term (*i.e.* term IV) is very close to 1:1, accounting for almost all of the total biases, whereas T_a variance term (*i.e.* Term III) and H.O.T. (*i.e.* Term V) are close to zeros and only become nontrivial at the annual timescale. Therefore, this analysis, using ERA-5 data, highlights the significance of temperature–radiation variances in estimating equilibrium evaporation, particularly at annual scale.

This dominant covariance term seems to be often positive (see Fig. 2a–c), which can be explained by the signs of both the derivative and the covariance. Solar radiation warms the Earth's surface and increases the air temperature, thus often leading to the positive correlation between radiation and temperature at various timescales, $\mathrm{cov}(T_a, Q) > 0$. The derivative, expressed as

$$f_{T_a,Q} = \frac{d}{dT_a}\frac{\Delta}{\lambda_w(\Delta+\gamma)}, \tag{7}$$

is also positive because of the monotonically increasing functions of $\Delta/(\Delta+\gamma)$ and $\Delta(T_a)$. Therefore, the covariance term often results in underestimation of equilibrium evaporation for applying Penman equation at different timescales.

Following the same approach for analyzing $\mathcal{F}_{P,e}$, we calculate each term in Eq. (5) using ERA-5 (see Fig. 1 d–f). Overall, the biases due to timescale mismatch due to drying power of the air, $\mathcal{F}_{P,d}$, are much larger than those from the equilibrium counterpart, $\mathcal{F}_{P,e}$ (also see Table 1). Similarly to the results in $\mathcal{F}_{P,e}$, the biases in $\mathcal{F}_{P,d}$ are also smaller at daily and monthly timescales than those at annual timescales.

To investigate the significance of each term in Eq. (5), we compared each term against the total bias (*i.e.* Term III+IV+V+VI+VII). Overall, terms III–VI are an order of magnitude smaller than terms V–VI; term III and term VI are usually positive; term IV and term V are often negative; the higher-order term is relatively small. While there is no single term that fits the total biases well, the majority of the biases are close to the combination of terms V and VI (see Fig. 2d–f), which is associated with the T_a-VPD and g_a-VPD covariances. These terms change from positive values in most daily cases to negative values in most annual cases, resulting in slight underestimation of daily PET and overestimation of annual PET (see bias statistics in Table 1).

3.2. Nonlinearity of Penman–Monteith equation

For the Penman–Monteith equation, we split $\mathcal{F}_{PM}$ into $\mathcal{F}_{PM,e}$ and $\mathcal{F}_{PM,d}$ and compared them with the corresponding first-order approximations at DMA timescales in Fig. 3. As can be seen, data points for $\mathcal{F}_{PM,e}$ are more scattered at daily and monthly timescales than those at annual timescale, whereas they are less scattered for $\mathcal{F}_{PM,d}$ at monthly timescale than those at daily and annual timescales. The overall biases at daily timescale in terms of root mean square bias (RMSB, see Appendix C) for $\mathcal{F}_{PM}$ are larger than those at monthly and annual timescales (see Table 1). The averages of the biases in terms of MB (see Appendix C) are positive at all timescales, suggesting first-order approximations of Penman–Monteith usually underestimate ET.

Due to the complexity of the Penman–Monteith equation, it is not practical to Taylor expand the biases into different terms as was done for the Penman equation in Section 3.1. Given the importance of covariance terms in the Penman equation, we also explored the relationship between the total biases (*i.e.*, H.O.T. in Eq. (6)) and some covariances between the input variables in the Penman–Monteith equation (see Table 2). While all these relationships are statistically significant, T_a-Q, T_a-V, and g_a-V covariances, as the primary sources of biases in the approximations of Penman equation, seem to be less important than the covariances between g_s and other meteorological variables. Particularly, g_s-V covariances are highly correlated with the total biases, whereas g_s-T_a and g_s-Q covariances are relatively larger at daily and monthly timescales, exhibiting complex nonlinear behavior at different temporal scales.

Table 2
Correlation coefficients between total biases (*i.e.*, H.O.T. in Eq. (6)) and some covariance terms in the Penman–Monteith equation. All coefficients are statistically significant (α = 0.05, two-tailed Student-t test)

Time scales	cov(T_a, Q)	cov(T_a, V)	cov(g_a, V)	cov(g_s, Q)	cov(g_s, V)	cov(g_s, T_a)	cov(g_s, g_a)
Daily	0.67	0.24	0.50	0.66	0.72	0.70	0.60
Monthly	0.63	0.11	0.49	0.70	0.72	0.71	0.67
Annual	0.41	−0.20	0.14	0.57	0.70	0.58	0.58

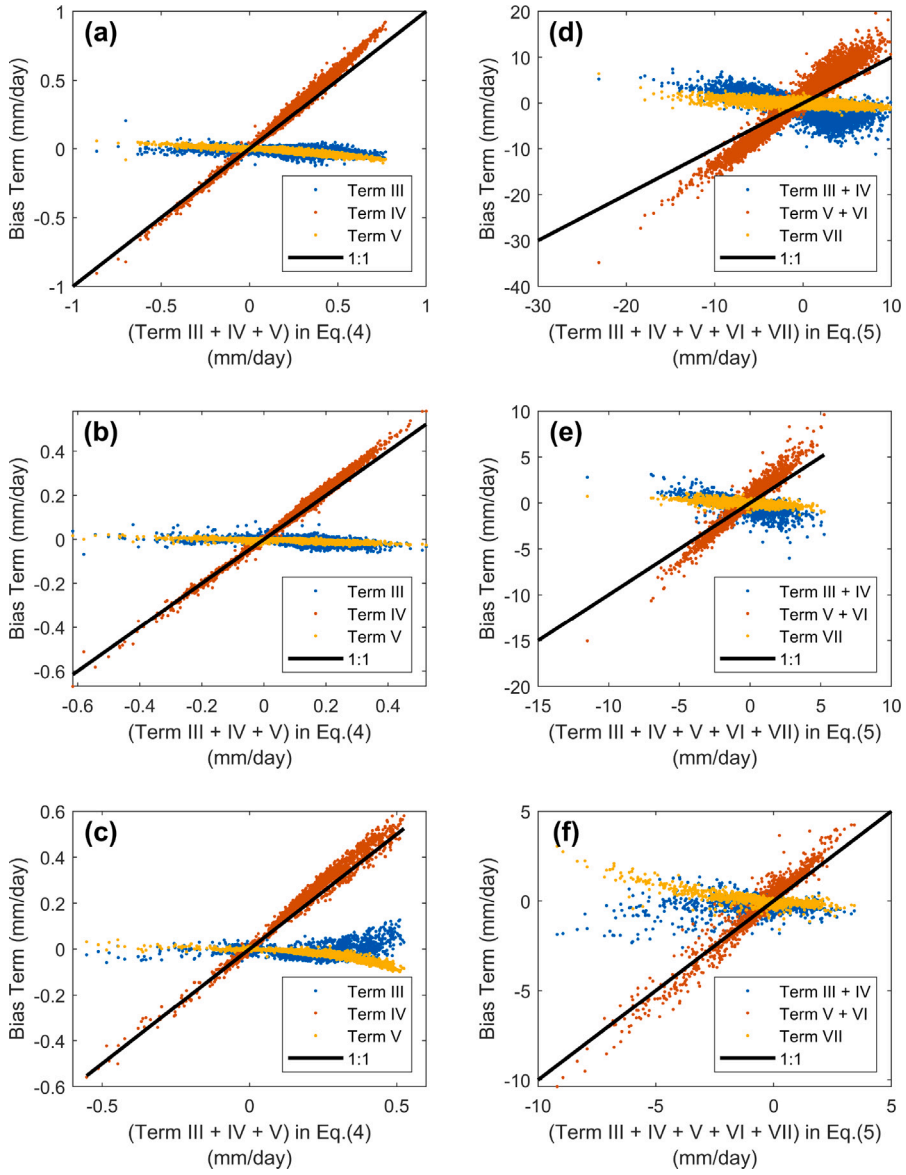

Fig. 2. Comparison of the bias terms with the total bias for approximating Penman equation at varying timescales. In panels (a)–(c), the bias terms in Eq. (4) are compared with the corresponding total bias at (a) daily, (b) monthly, and (c) annual timescales, respectively. In panels (d)–(f), the bias terms in Eq. (5) are compared with the total bias at (d) daily, (e) monthly, and (f) annual scales, respectively. See data source in Section 2.3.

3.3. Spatial distribution of biases

Both Penman and Penman–Monteith equations have shown certain biases when applied at DMA timescales. Overall, the average biases measured by RMSB for approximating the Penman equation range from 0.72 to 1.31 mm day^{-1}, and the average biases for approximating the Penman–Monteith equation vary from 0.47 to 0.53 mm day^{-1}. As a reference, the global averages from Penman and Penman–Monteith equation at hourly timescale over the year 1994 are 7.1 and 1.7 mm/day. It should be noted that PET estimated here with consideration of the atmospheric stability tends to be larger than those without stability correction (Mahrt and Ek, 1984). This suggests high nonlinearities of Penman and Penman–Monteith equations and thus advises its application over long temporal scales with extra caution.

An advantage of using available climatological data is that we can readily geolocate biases, especially the large biases. As shown in Fig. 4, the regions of large biases at daily, monthly, and annual timescales were found across various climate zones. This is also consistent with previous studies which found large biases in China, Australia, and the United States (Yang and Zhong, 2011; Perera et al., 2015; Itenfisu et al., 2003; Suleiman and Hoogenboom, 2009). For PET estimated by approximating the Penman equation at daily timescale, there are large

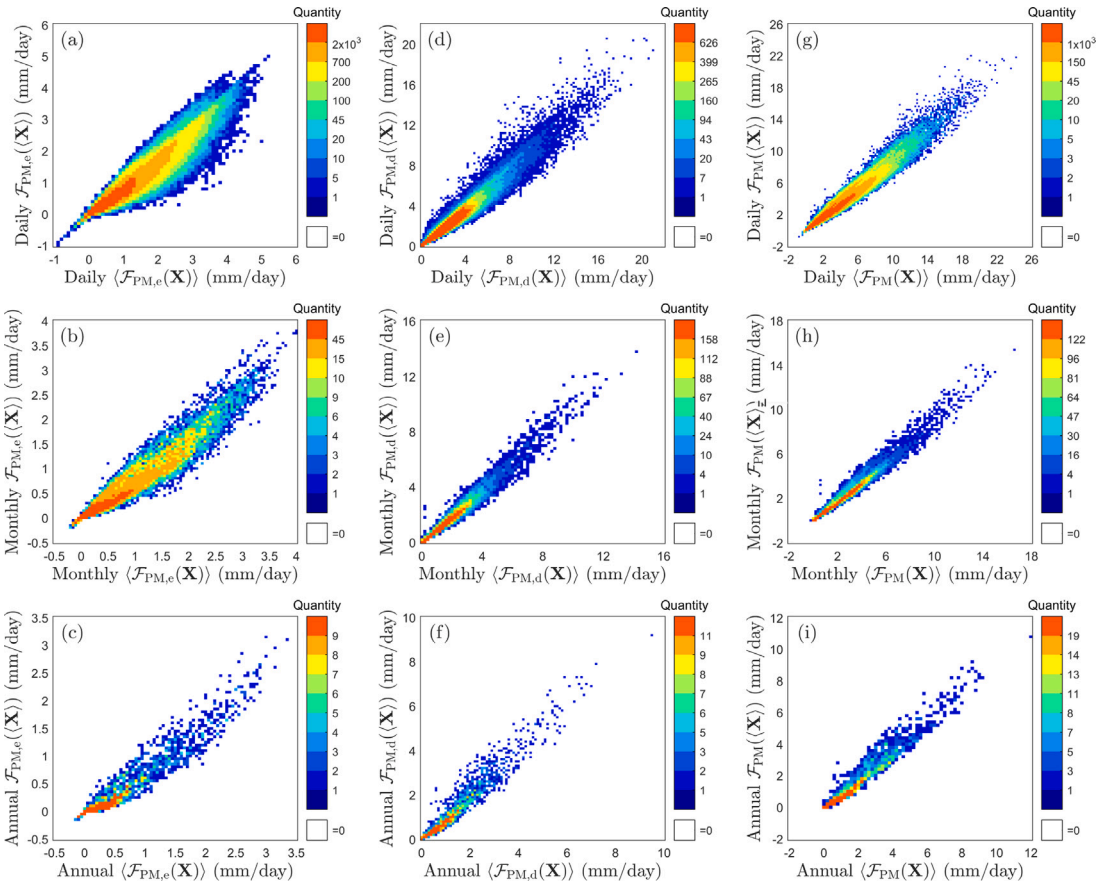

Fig. 3. Approximations of Penman–Monteith equation at varying timescales. In panels (a)–(c), the exact values, $\langle \mathcal{F}_{PM,e}(\mathbf{X}) \rangle$, are compared with first-order approximations, $\mathcal{F}_{PM,e}(\langle \mathbf{X} \rangle)$, at the (a) daily, (b) monthly, and (c) annual scales, respectively. In panels (d)–(f), the exact values, $\langle \mathcal{F}_{PM,d}(\mathbf{X}) \rangle$, are compared with the first-order approximations, $\mathcal{F}_{PM,d}(\langle \mathbf{X} \rangle)$, at the (d) daily, (e) monthly, and (f) annual scales, respectively. In panels (g)–(i), the exact values, $\langle \mathcal{F}_{PM}(\mathbf{X}) \rangle$ are compared with the first order approximation $\mathcal{F}_{PM}(\langle \mathbf{X} \rangle)$ at (g) daily, (h) monthly, and (i) annual timescales. The vector $\mathbf{X}$ refers to the list of variables in the corresponding functions; $\langle \mathcal{F}(\cdot) \rangle$ refers to the average of the function; $\mathcal{F}(\langle \cdot \rangle)$ refers to the function of the averages. Note that there are 2337 resampled locations over the global land and the total sample sizes are 365×2337, 12×2337, and 2337 at DMA timescales (also see data source in Section 2.3). The quantity color bars show the numbers of the samples.

biases in Asia, Southern Africa, and coastal regions of the Americas. This gradually shifts towards Europe, Northern Asia, and Canada at monthly and annual timescales. For ET estimated by approximating the Penman–Monteith equation, large biases are located around Southern Africa, South Asia, Australia, and Americas.

To interpret this global pattern, we focused on the major bias sources, which are T_a-Q, T_a-V, g_a-V covariances for the Penman equation and also include g_s-V covariance for the Penman–Monteith equation. As shown in Fig. 5, larger T_a-Q covariances can be found in temperate and cold regions, where the local surface heating may be one of the most important sources for warming the atmosphere air. For T_a-V covariances, the large values are often found in dry regions, where the nonlinear relationship between temperature and saturation vapor pressure may be responsible for the variations in VPD. For g_a-V, their covariances are more prominent in the tropics and Southern Hemisphere. The covariances of g_s-V related to the Penman–Monteith equation are more negative around the Sahel region, Mideast, and South Asia. This implies that the biases present in various regions are linked to distinct climate forcing factors, hence requiring particular attention for applying these equations at long timescales.

The biases from the first-order approximation of PET could influence the estimation of the dryness index (= PET/P), which has been extensively used in a wide range of hydrological, climatological, and biogeochemical applications (e.g., Arora, 2002; Zarch et al., 2015; Greve et al., 2019; Calabrese and Porporato, 2020; Porporato, 2021; Huang et al., 2023). To explore this effect, we compared the global dryness index based on both accurate PET and its first-order approximations (see Fig. 6). Overall, the dryness index biases are larger in dry regions, where the low precipitation in the denominator of the dryness index (= PET/P) tends to amplify the biases. The small biases in the climate transitional zone also should not be ignored, as the small variations in dryness index potentially shift the hydrological processes from water-limit to energy-limit regimes. These biases at annual scales are relatively larger than those at daily and monthly scales, consistent with the corresponding PET biases.

4. Conclusions

In this study, we explored the nonlinearities of Penman and Penman–Monteith equations to address the potential biases associated with timescale mismatches. We Taylor expanded Penman and Penman–Monteith equations to compare their first-order approximations with the corresponding variance, co-variance, and higher-order terms. Using the state-of-the-art global reanalysis data, we found that the biases from approximating equilibrium evapotranspiration from the Penman equation mainly come from the temperature–radiation covariance term, whereas the biases from approximating evaporation due to the drying power of the air are primarily associated with covariances between temperature and VPD and between aerodynamic conductance and VPD. Relatively larger biases were observed in approximating the Penman–Monteith equation for the calculation of ET from a non-wet surface, as the addition of stomatal conductance, probably due to its covariance with VPD, significantly increases the nonlinearity of the Penman–Monteith equation.

The biases can be larger in certain regions across different climate zones, where distinct climate forcings tend to have one or multiple

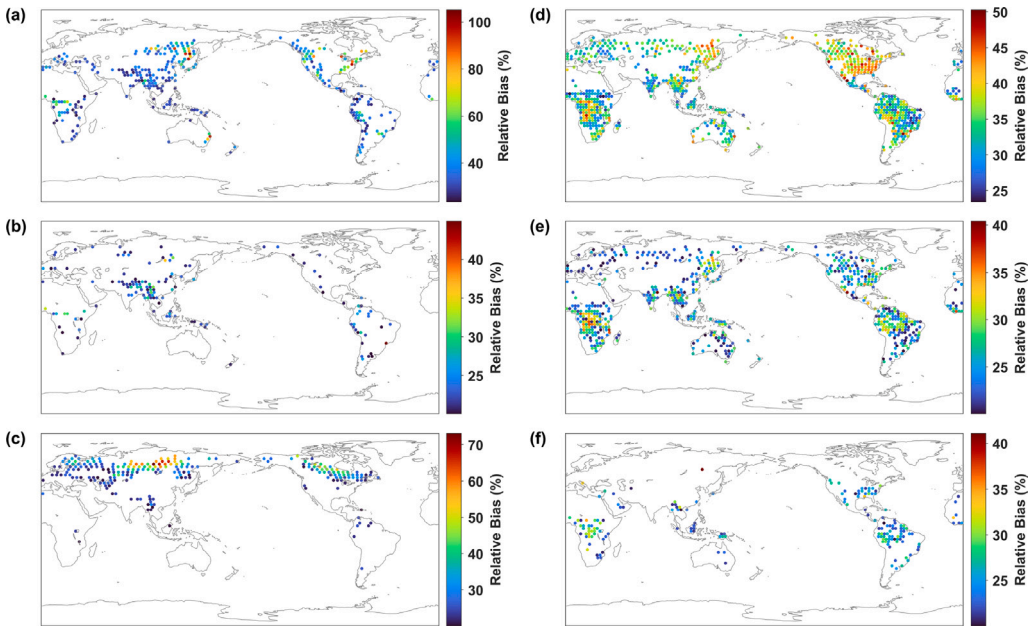

Fig. 4. Spatial distribution of large biases (a, b, c) for approximating Penman and (d, e, f) Penman–Monteith equations. The dots indicate that the number of the cases with 20% or larger relative biases and ET > 3 mm day^{-1} or PET > 3 mm day^{-1} is larger than 30 at (a, d) daily scales and larger than or equal to one at (b, e) monthly and (c, f) annual scales.

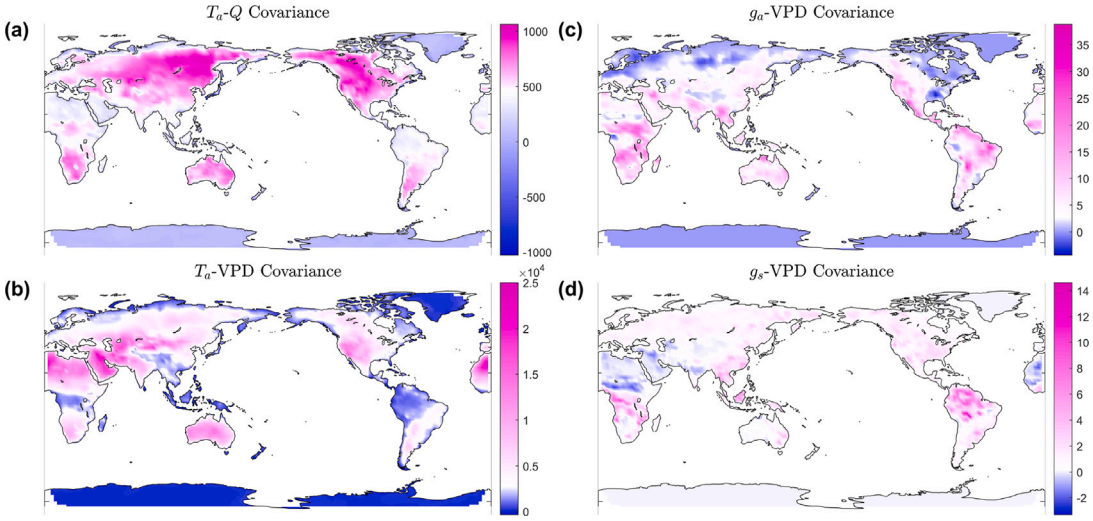

Fig. 5. Global distributions of (a) T_a-Q, (b) T_a-VPD, (c) g_a-VPD, and (d) g_s-VPD covariances calculated from hourly time series of T_a, Q, VPD, g_a, g_s over the whole year of 1994.

higher covariances among different meteorological variables and thus makes these first-order approximations less accurate. It also important to note that the relationships among temperature, radiation, humidity, and wind are not necessarily the same under changing climates. Global warming tends to increase day and night temperatures at different rates (Cox et al., 2020) and alter the tropospheric stability (Ceppi and Gregory, 2017), resulting in changes in the dynamics of the atmosphere boundary layer and the diurnal variations of atmospheric humidity. Variations in these hydrometeorological variables may lead to changes in biases. Caution should be exercised when using daily, monthly, or annual climate model outputs to calculate global evaporation under future scenarios, which may result in an inaccurate assessment of the future water cycle.

Interestingly, there may also be a problem of "spatial scale mismatch" when applying Penman and Penman–Monteith equations. Each grid point in ERA-5 datasets has a resolution of 0.25°, within which land use and land cover is not necessarily homogeneous. Using spatially averaged meteorological variables in each grid point as inputs for Penman and Penman–Monteith equations may in fact introduce biases. Future analyses through comparison between site observations and these grid data may provide insight into this "spatial scale mismatch" problem.

Finally, it should be kept in mind that this study focused on the Penman and Penman–Monteith equations and did not address biases associated with the original assumptions behind these equations, such as linearization of saturation vapor pressure and saturated conditions inside the stomates of non-wet surfaces. It is estimated that the Penman equation with linearized saturation vapor pressure curve consistently underestimates evaporation and the relative biases in certain extreme cases can be as high as 10% (Paw U and Gao, 1988; Milly, 1991;

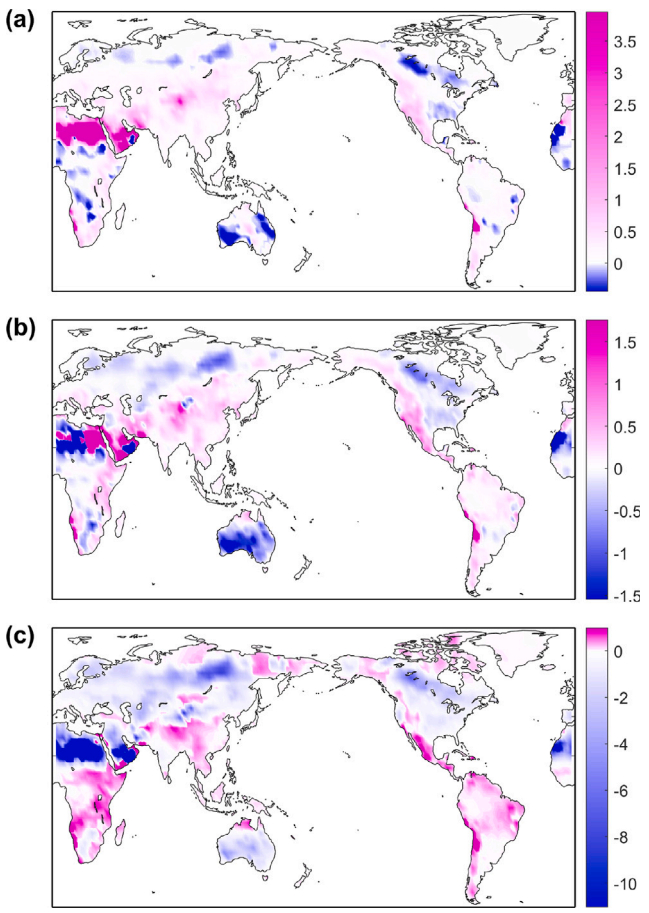

Fig. 6. Differences in dryness index (= PET/P) with PET calculated from the Penman equation and its first-order approximation at daily (a), monthly (b), and annual (c) timescales. The precipitation (P) and meteorological variables for Penman equations are from ERA-5 reanalysis over the whole year of 1994.

McColl, 2020). Using global meteorological data, it is estimated that the overall biases are around 0.1 mm/day, approximately 2.4% of the annual PET (Liu et al., 2021). Exploration of these assumptions and the use of other comprehensive datasets at high spatial and temporal resolutions may be an interesting future extension of this work.

CRediT authorship contribution statement

Yizhi Han: Writing – review & editing, Writing – original draft, Visualization, Validation, Software, Methodology, Formal analysis, Data curation. **Salvatore Calabrese:** Writing – review & editing, Visualization, Methodology, Investigation, Formal analysis, Conceptualization. **Huihua Du:** Writing – review & editing, Methodology, Formal analysis. **Jun Yin:** Writing – review & editing, Supervision, Resources, Project administration, Methodology, Funding acquisition, Formal analysis, Data curation, Conceptualization.

Declaration of competing interest

The authors declare that they have no known competing financial interests or personal relationships that could have appeared to influence the work reported in this paper.

Data availability

ERA5 datasets are available at https://cds.climate.copernicus.eu/cdsapp#!/dataset/reanalysis-era5-single-levels.

Acknowledgments

J.Y. acknowledges support from the Natural Science Foundation of Jiangsu Province (BK20221343). S.C. was supported by the National Science Foundation (DEB-2213630), the USDA National Institute of Food and Agriculture (Hatch project 1023954), and the Department of Biological and Agricultural Engineering and AgriLife Research at Texas A&M University. The comments and useful suggestions from five anonymous reviewers, editor, and associate editor are gratefully acknowledged.

Appendix A. Turbulent transport of surface heat fluxes

The Penman and Penman–Monteith equations were derived from the turbulent transport of latent and sensible heat fluxes from the surface to the atmosphere (Stull, 1988; Garratt, 1994; Brutsaert, 2013; Porporato and Yin, 2022)

$$H = \rho c_p \overline{w'T'} = \rho c_p g_a (T_0 - \overline{T_a}) \tag{A.1}$$

$$\rho_w E = \rho \overline{w'q'} = \rho \frac{g_a g_s}{g_a + g_s} \frac{\epsilon}{p_0} \left[e_0 - \overline{e}_a \right] \tag{A.2}$$

where H is sensible heat flux, E is evapotranspiration rate, c_p is specific heat capacity, ρ_w is water density, ρ is the air density, ϵ (≈ 0.622) is the ratio of the water and air molar masses, p_0 is atmospheric pressure, e is vapor pressure, $q (\approx \epsilon e / p_0)$ is specific humidity, T_0 is the surface temperature, the bars indicate Reynolds averages at timescale of half hour to an hour (Stull, 1988), and subscripts 0 and a refer the corresponding variables at the surface and in the atmosphere (*e.g.*, low level of the mixing layer), T_a and e_a are temperature and vapor pressure in the atmosphere, and g_a and g_s are the aerodynamic and stomatal (or canopy) conductances. While there are various models for simulating aerodynamic conductance (see a list in Liu et al., 2007), we followed the Monin–Obukhov similarity theory and modeled g_a as (ECMWF, 2023) Eq. (A.3) given in Box I where κ is the von Karman constant, $\bar{u}_a$ is wind speed at z_a, z_{0M} and z_{0H} are the momentum and thermal roughness heights, Ψ_M and Ψ_H are the stability correction functions for momentum and heat transfer, L is the Monin–Obukhov length. We followed ECMWF (2023) and used the correction functions given by Paulson (1970) for unstable conditions and the correction functions by Holtslag and De Bruin (1988) for stable situations. The stomatal conductance, g_s, refers to the controls of leaf stomatal openings to the water flux for vegetated surface and is treated as a limiting factor from unsaturated soil for non-vegetated areas,

$$g_s = c g_{s,\max} f_1(R_s) f_2(s_r) f_3(V) + (1 - c) g_{\text{soil},\max} f_4(s_1), \tag{A.4}$$

where c is vegetation coverage, $g_{s,\max}$ is the maximum stomatal conductance for the given vegetation, R_s is the downward shortwave radiation, s_r and s_1 are the root-zone and surface-layer soil moisture, V is vapor pressure deficit, and $g_{\text{soil},\max}$ is the maximum conductance from bare soil surface with a typical value of 0.02 ms^{-1}, f_1, f_2, f_3, and f_4 are the empirical functions modeling the impacts of each variable (ECMWF, 2023).

For wet surfaces with high stomatal conductance ($g_s \gg g_a$), one finds the explicit expression for ET in Eq. (1) by solving Eqs. (A.1) and (A.2) with surface energy balance equation and linearized saturation vapor pressure curve. For non-wet surface with an assumption of $e_0 = e_{\text{sat}}(T_0)$, a similar expression for ET can be derived as in Eq. (3).

Appendix B. Taylor series for multivariable functions

Application of Penman equation at a longer timescale should proceed with caution. To explain this point, we consider the general case of two nonlinear functions, $h(x, y)$ and $h(x, y, z)$. Taylor expanding the

$$g_a = \frac{\bar{u}_a \kappa^2}{\left[\ln\left(\frac{z_a+z_{0M}}{z_{0M}}\right) - \Psi_M\left(\frac{z_a+z_{0M}}{L}\right) + \Psi_M\left(\frac{z_{0M}}{L}\right)\right]\left[\ln\left(\frac{z_a+z_{0M}}{z_{0H}}\right) - \Psi_H\left(\frac{z_a+z_{0M}}{L}\right) + \Psi_H\left(\frac{z_{0H}}{L}\right)\right]}, \tag{A.3}$$

Box I.

first function at the mean values of x and y, and the second one at the mean values of x, y and z gives

$$\begin{aligned} h(x,y) = {} & h(\langle x\rangle,\langle y\rangle) + (x-\langle x\rangle)h_x + (y-\langle y\rangle)h_y \\ & + 1/2(x-\langle x\rangle)^2 h_{xx} + 1/2(y-\langle y\rangle)^2 h_{yy} \\ & + (x-\langle x\rangle)(y-\langle y\rangle)h_{xy} + \text{H.O.T.}, \end{aligned} \tag{B.1}$$

and

$$\begin{aligned} h(x,y,z) = {} & h(\langle x\rangle,\langle y\rangle,\langle z\rangle) + (x-\langle x\rangle)h_x \\ & + (y-\langle y\rangle)h_y + (z-\langle z\rangle)h_z + 1/2(x-\langle x\rangle)^2 h_{xx} \\ & + 1/2(y-\langle y\rangle)^2 h_{yy} + 1/2(z-\langle z\rangle)^2 h_{zz} \\ & + (x-\langle x\rangle)(y-\langle y\rangle)h_{xy} + (x-\langle x\rangle)(z-\langle z\rangle)h_{xz} \\ & + (y-\langle y\rangle)(z-\langle z\rangle)h_{yz} + \text{H.O.T.}, \end{aligned} \tag{B.2}$$

where $\langle x\rangle$, $\langle y\rangle$ and $\langle z\rangle$, different from Reynolds averages, refer to the averages of x, y, z for any given period, function h with subscripts are the corresponding derivatives evaluated at $(\langle x\rangle,\langle y\rangle)$ or $(\langle x\rangle,\langle y\rangle,\langle z\rangle)$, and H.O.T. are higher-order Taylor series terms. Applying averages for the whole equations ((B.1) and (B.2)) yields

$$\begin{aligned} \langle h(x,y)\rangle = {} & h(\langle x\rangle,\langle y\rangle) + 1/2h_{xx}\sigma_x^2 + 1/2h_{yy}\sigma_y^2 \\ & + h_{xy}\text{cov}(x,y) + \langle\text{H.O.T.}\rangle, \end{aligned} \tag{B.3}$$

and

$$\begin{aligned} \langle h(x,y,z)\rangle = {} & h(\langle x\rangle,\langle y\rangle,\langle z\rangle) + 1/2h_{xx}\sigma_x^2 + 1/2h_{yy}\sigma_y^2 \\ & + 1/2h_{zz}\sigma_z^2 + h_{xy}\text{cov}(x,y) + h_{xz}\text{cov}(x,z) \\ & + h_{yz}\text{cov}(y,z) + \langle\text{H.O.T.}\rangle, \end{aligned} \tag{B.4}$$

where σ_x, σ_y and σ_z are standard deviations of x, y and z, $\text{cov}(x,y)$ is the covariance of x and y; similarly, $\text{cov}(x,z)$ and $\text{cov}(y,z)$ are the covariances of the corresponding variables. In linear system, *e.g.*, $h(x,y) = x+y$, Eq. (B.3) is reduced to $\langle h(x,y)\rangle = h(\langle x\rangle,\langle y\rangle)$, and for $h(x,y,z) = x+y+z$, Eq. (B.4) is reduced to $\langle h(x,y,z)\rangle = h(\langle x\rangle,\langle y\rangle,\langle z\rangle)$; in multiplicative system, *e.g.*, $h(x,y) = xy$, Eq. (B.3) is reduced to $\langle h(x,y)\rangle = h(\langle x\rangle,\langle y\rangle) + h_{xy}\text{cov}(x,y)$, and for $h(x,y,z) = xyz$, Eq. (B.4) is reduced to $\langle h(x,y,z)\rangle = h(\langle x\rangle,\langle y\rangle) + h_{xy}\text{cov}(x,y) + h_{xz}\text{cov}(x,z) + h_{yz}\text{cov}(y,z)$; for Penman equation, most terms in Eq. (B.3) and (B.4) reserve.

Appendix C. Bias statistics

To quantify the differences between the approximate values and the exact values over a sample of size n, we used three statistical indices, namely root mean square bias (RMSB), mean absolute bias (MAB), and mean bias (MB). The formulas are as follows,

$$\text{RMSB} = \sqrt{\frac{1}{n}\sum_{i=1}^{n}\left(Y_{e,i} - Y_{a,i}\right)^2}, \tag{C.1}$$

$$\text{MAB} = \frac{1}{n}\sum_{i=1}^{n}|Y_{e,i} - Y_{a,i}|, \tag{C.2}$$

and

$$\text{MB} = \frac{1}{n}\left(\sum_{i=1}^{n}Y_{e,i} - \sum_{i=1}^{n}Y_{a,i}\right), \tag{C.3}$$

where a set of exact value $Y_{e,i}$ of size n is compared with the corresponding approximation, $Y_{a,i}$.

References

Allen, R.G., Pereira, L.S., Raes, D., Smith, M., et al., 1998. Crop evapotranspiration-guidelines for computing crop water requirements-FAO irrigation and drainage paper 56. Fao, Rome 300 (9), D05109.

Arora, V.K., 2002. The use of the aridity index to assess climate change effect on annual runoff. J. Hydrol. 265 (1–4), 164–177. http://dx.doi.org/10.1016/s0022-1694(02)00101-4.

Brutsaert, W., 2013. Evaporation into the Atmosphere: Theory, History and Applications, vol. 1, Springer Science & Business Media.

Cai, J., Liu, Y., Lei, T., Pereira, L.S., 2007. Estimating reference evapotranspiration with the FAO Penman–Monteith equation using daily weather forecast messages. Agricult. Forest. Meterol. 145 (1–2), 22–35.

Calabrese, S., Porporato, A., 2020. Wetness controls on global chemical weathering. Environ Res Commun 2 (8), 085005. http://dx.doi.org/10.1088/2515-7620/abad7b.

Ceppi, P., Gregory, J.M., 2017. Relationship of tropospheric stability to climate sensitivity and earth's observed radiation budget. Proc. Natl. Acad. Sci. 114 (50), 13126–13131. http://dx.doi.org/10.1073/pnas.1714308114.

Cox, D.T., Maclean, I.M., Gardner, A.S., Gaston, K.J., 2020. Global variation in diurnal asymmetry in temperature, cloud cover, specific humidity and precipitation and its association with leaf area index. Global Change Biol. 26 (12), 7099–7111.

Dai, A., 2023. The diurnal cycle from observations and ERA5 in surface pressure, temperature, humidity, and winds. Clim. Dyn. 1–26.

ECMWF, 2023. IFS Documentation – Cy48r1: Part IV: Physical Processes. Technical Report, ECMWF, http://dx.doi.org/10.21957/02054f0fbf.

Fick, S.E., Hijmans, R.J., 2017. WorldClim 2: New 1-km spatial resolution climate surfaces for global land areas. Int. J. Climatol. 37 (12), 4302–4315.

Garratt, J.R., 1994. The atmospheric boundary layer. Earth-Sci. Rev. 37 (1–2), 89–134.

Greve, P., Roderick, M.L., Ukkola, A.M., Wada, Y., 2019. The aridity index under global warming. Environ. Res. Lett. 14 (12), 124006. http://dx.doi.org/10.1088/1748-9326/ab5046.

Harris, I., Osborn, T.J., Jones, P., Lister, D., 2020. Version 4 of the CRU TS monthly high-resolution gridded multivariate climate dataset. Sci. Data 7 (1), 109.

Hersbach, H., Bell, B., Berrisford, P., Hirahara, S., Horányi, A., Muñoz-Sabater, J., Nicolas, J., Peubey, C., Radu, R., Schepers, D., Simmons, A., Soci, C., Abdalla, S., Abellan, X., Balsamo, G., Bechtold, P., Biavati, G., Bidlot, J., Bonavita, M., De Chiara, G., Dahlgren, P., Dee, D., Diamantakis, M., Dragani, R., Flemming, J., Forbes, R., Fuentes, M., Geer, A., Haimberger, L., Healy, S., Hogan, R.J., Hólm, E., Janisková, M., Keeley, S., Laloyaux, P., Lopez, P., Lupu, C., Radnoti, G., de Rosnay, P., Rozum, I., Vamborg, F., Villaume, S., Thépaut, J.-N., 2020. The ERA5 global reanalysis. Q. J. R. Meteorol. Soc. 146 (730), 1999–2049. http://dx.doi.org/10.1002/qj.3803.

Hoffmann, L., Günther, G., Li, D., Stein, O., Wu, X., Griessbach, S., Heng, Y., Konopka, P., Müller, R., Vogel, B., et al., 2019. From ERA-interim to ERA5: The considerable impact of ECMWF's next-generation reanalysis on Lagrangian transport simulations. Atmos. Chem. Phys. 19 (5), 3097–3124.

Holtslag, A., De Bruin, H., 1988. Applied modeling of the nighttime surface energy balance over land. J. Appl. Meteorol. Climatol. 27 (6), 689–704.

Huang, H., Wu, J., Calabrese, S., 2023. Emergent climatic controls on soil carbon turnover and its variability in warm climates. Geophys. Res. Lett. 50 (22), http://dx.doi.org/10.1029/2023gl105291.

Huang, J., Yu, H., Guan, X., Wang, G., Guo, R., 2015. Accelerated dryland expansion under climate change. Nature Clim. Change 6 (2), 166–171. http://dx.doi.org/10.1038/nclimate2837.

Itenfisu, D., Elliott, R.L., Allen, R.G., Walter, I.A., 2003. Comparison of reference evapotranspiration calculations as part of the ASCE standardization effort. J. Irrig. Drain. Eng. 129 (6), 440–448.

Lhomme, J.-P., 1997. Towards a rational definition of potential evaporation. Hydrology and Earth System Sciences 1 (2), 257–264. http://dx.doi.org/10.5194/hess-1-257-1997.

Liu, S., Lu, L., Mao, D., Jia, L., 2007. Evaluating parameterizations of aerodynamic resistance to heat transfer using field measurements. Hydrol. Earth Syst. Sci. 11 (2), 769–783.

Liu, M., Xu, X., Scanlon, B.R., Sun, A.Y., Wang, K., 2021. A modified evaporation model indicates that the effects of air warming on global drying trends have been overestimated. J. Geophys. Res.: Atmos. 126 (22), http://dx.doi.org/10.1029/2021jd035153.

Mahrt, L., Ek, M., 1984. The influence of atmospheric stability on potential evaporation. J. Clim. Appl. Meteorol. 23 (2), 222–234. http://dx.doi.org/10.1175/1520-0450(1984)023<0222:tioaso>2.0.co;2.

McColl, K.A., 2020. Practical and theoretical benefits of an alternative to the Penman-Monteith evapotranspiration equation. Water Resour. Res. 56 (6), e2020WR027106.

Milly, P., 1991. A refinement of the combination equations for evaporation. Surv. Geophys. 12 (1–3), 145–154.

Monteith, J.L., 1965. Evaporation and environment. In: Symposia of the Society for Experimental Biology, vol. 19, Cambridge University Press (CUP) Cambridge, pp. 205–234.

Pastorello, G., Trotta, C., Canfora, E., Chu, H., Christianson, D., Cheah, Y.W., Poindexter, C., Chen, J., Elbashandy, A., Humphrey, M., et al., 2020. The FLUXNET2015 dataset and the ONEFlux processing pipeline for eddy covariance data. Sci. Data 7 (1), 1–27.

Paulson, C.A., 1970. The mathematical representation of wind speed and temperature profiles in the unstable atmospheric surface layer. J. Appl. Meteorol. Climatol. 9 (6), 857–861.

Paw U, K.T., Gao, W., 1988. Applications of solutions to non-linear energy budget equations. Agricult. Forest. Meterol. 43 (2), 121–145. http://dx.doi.org/10.1016/0168-1923(88)90087-1.

Penman, H.L., 1948. Natural evaporation from open water, bare soil and grass. Proc. R. Soc. Lond. Ser. A. Math. Phys. Sci. 193 (1032), 120–145.

Perera, K.C., Western, A.W., Nawarathna, B., George, B., 2015. Comparison of hourly and daily reference crop evapotranspiration equations across seasons and climate zones in Australia. Agricult. Water. Manag. 148, 84–96.

Porporato, A., 2021. Hydrology without dimensions. http://dx.doi.org/10.5194/hess-2021-442.

Porporato, A., Yin, J., 2022. Ecohydrology: Dynamics of Life and Water in the Critical Zone. Cambridge University Press.

Song, Y.H., Chung, E.-S., Shahid, S., Kim, Y., Kim, D., 2023. Development of global monthly dataset of CMIP6 climate variables for estimating evapotranspiration. Sci. Data 10 (1), 568.

Stull, R.B., 1988. An Introduction to Boundary Layer Meteorology. Kluwer Academic Publishers.

Suleiman, A.A., Hoogenboom, G., 2007. Comparison of Priestley-Taylor and FAO-56 Penman-Monteith for daily reference evapotranspiration estimation in Georgia. J. Irrig. Drain. Eng. 133 (2), 175–182. http://dx.doi.org/10.1061/(asce)0733-9437(2007)133:2(175).

Suleiman, A.A., Hoogenboom, G., 2009. A comparison of ASCE and FAO-56 reference evapotranspiration for a 15-min time step in humid climate conditions. J. Hydrol. 375 (3–4), 326–333.

Wang, X., Jiang, D., Lang, X., 2020. Future changes in Aridity Index at two and four degrees of global warming above preindustrial levels. Int. J. Climatol. 41 (1), 278–294. http://dx.doi.org/10.1002/joc.6620.

Wild, M., Ohmura, A., Schär, C., Müller, G., Folini, D., Schwarz, M., Hakuba, M.Z., Sanchez-Lorenzo, A., 2017. The global energy balance archive (GEBA) version 2017: A database for worldwide measured surface energy fluxes. Earth Syst. Sci. Data 9 (2), 601–613.

Yang, X., Zhong, P., 2011. Comparative analysis on reference crop evapotranspiration based on two different time steps meteorological data. Chin. J. Agrometeorol. 32 (02), 214.

Zarch, M.A.A., Sivakumar, B., Sharma, A., 2015. Assessment of global aridity change. J. Hydrol. 520, 300–313. http://dx.doi.org/10.1016/j.jhydrol.2014.11.033.

Zomer, R.J., Xu, J., Trabucco, A., 2022. Version 3 of the global aridity index and potential evapotranspiration database. Sci. Data 9 (1), 409.